Li, M., et al. On the electron boundary conditions in PIC plasma thruster plume simulations, In: *Plasma sources science and technology, 28, 034004, March 2019, 12 Pp.*

DOI: https://doi.org/10.1088/1361-6595/ab0949

On the electron boundary conditions in full PIC simulations of plasma thruster plumes

Min Li,[1,*] Mario Merino,[2,†] Eduardo Ahedo,[2,‡] and Haibin Tang[3,4,§]

[1] *School of Astronautics, Beihang University, Beijing, China*
[2] *Equipo de Propulsión Espacial y Plasmas (EP2), Universidad Carlos III de Madrid, Leganés, Spain*
[3] *School of Space and Environment, Beihang University, Beijing, China*
[4] *Key Laboratory of Spacecraft Design Optimization & Dynamic Simulation Technologies, Ministry of Education, China*

The collisionless, steady state expansion into vacuum of a warm electron, cold ion plasma thruster plume is studied with a set of new electrostatic particle-in-cell model and globally-consistent boundary conditions that discriminate between reflected and escaping electrons. As a proof of concept, several simulations are analyzed. Results from both two-dimensional planar and axisymmetric plasma plumes are discussed. In particular, the electrons' anisothermal and anisotropic behavior in the plume is recovered.

Keywords: electric space propulsion, plasma plumes, particle in cell, simulation, boundary conditions

I. INTRODUCTION

The energetic plasma plumes created by electric propulsion (EP) devices remain a matter of essential engineering and scientific concern for space missions due to its potential interaction with the spacecraft. Consisting of charged and neutral particles of different species, the plume may impinge on spacecraft surfaces such as solar arrays and photosensitive components, causing chemical and physical damage[1–3]. Some of the possible phenomena include material/charge deposition, which directly contaminates sensitive surfaces, erosion and sputtering of softer materials, charging-discharging of dielectric components, additional heat loads to certain parts of the spacecraft, induction of electric and magnetic fields, and perturbation on the propagation of electromagnetic waves. To minimize these unfavorable interactions, both electric thruster designers and spacecraft system integrators need to understand the plasma environment as the jet expands from the exit of thruster into the vacuum of space. The expansion of plasma plumes, moreover, appears in other areas of plasma physics spanning from material processing of semiconductors to astrophysical phenomena[4–6].

Over the past decades, two of the leading types of EP thrusters have been the gridded ion thruster (GIT) and the Hall effect thruster (HET)[3, 7, 8]. Their plasma plumes are rarefied and hypersonic. They exhibit distinct characteristics in the near region right outside of the thruster, where collisions and 3D inhomogeneities are important, and in the far region, which starts a few thruster radii downstream from the thruster exit, where the expansion is smooth and near-collisionless[9–15]. The continued plume expansion in this latter region is mainly driven by the ion inertia and the residual electron thermal pressure[11, 14, 15].

Extensive numerical efforts devoted to the characterization of the properties of plasma thruster plumes can be found in the literature; see, for example, references [16–20] and those cited in [15, 21]. The treatment of electrons varies from kinetic (solving Vlasov-Boltzmann directly or using the Particle-in-Cell (PIC) method[22]) to fluid approximations that rely on an isothermal or polytropic closure of the equations. The fluid approach is used in codes such as EASYPLUME[15], which has been used to study the far-plume macroscopic properties. Fluid electrons are also part of hybrid codes, which solve heavy species (ions, neutrals) with the PIC method[23–26]. However, given the low collisionality in the plasma plume, there is no theoretical support for the usual fluid closure relations[15]. Consequently, a more desirable choice to explore the microscopic physical details of the plasma expansion is a full kinetic description of the electrons. Needless to say, the computational cost of full kinetic models is large, making it only affordable for particular studies in small domains, and remains impractical for large-scale simulations. One-dimensional direct-Vlasov models have recently helped identify the existence collisionless electron cooling and anisotropization mechanisms[21, 27]. The two-dimensional full PIC approach has proven capable of demonstrating the beam neutralization process and the new equilibrium of collisionless electrons during the transient set-up of a plasma plume[28–31].

In general the plasma thruster plume is quasineutral and most electrons are confined by the ambipolar electric field. This means that all electrons, except for the most energetic ones, are reflected back to the plasma source; moreover, some of the electrons may be trapped in the plume[21]. Some of these electrons may travel far downstream (and effectively beyond the simulation domain boundary) before being reflected; this is especially concerning when using small simulation domains to save computational resources. As a consequence, the widely-used simple open boundary condition, which eliminates all electrons leaving the finite simulation do-

* lm@buaa.edu.cn
† mario.merino@uc3m.es
‡ eduardo.ahedo@uc3m.es
§ thb@buaa.edu.cn, corresponding author

main, overestimates the free electron flow and is unlikely to represent a physically reasonable plasma expansion process. For this reason simulations are usually stopped before the leading edge of the plume reaches the boundary to prevent border effects and the unavoidable instabilities[28, 29]. Thus, up to now, only short-time, transient plume set-up simulations in small domains have been carried out; the full PIC study of the steady-state plume expansion remains an unsolved challenge. A recent study[32] has partially addressed these issues by setting up a virtual ion sink inside the domain and selecting a fraction of electrons that reach the boundaries to be reflected back based on their number and a global charge conservation criterion.

Clearly, setting the right boundary conditions (BCs) for a finite computational domain is crucial for simulation correctness, especially as the electron response is non-local. The boundary problem is twofold, in one respect relating to retaining the correct amount of electrons reaching the boundary, and in another to correctly treating the electric field at the border. Furthermore, the problem of escaping electrons is directly coupled to the injection of new particles in the domain and the current-free condition that must be satisfied by the typical plasma thruster plume.

This paper presents kinetically-consistent electron boundary conditions for steady-state full PIC simulations of plasma plumes with finite domains. These boundary conditions are implemented in a full PIC model that assumes a collisionless, unmagnetized, and current-free plasma expansion into vacuum, which accounts for the far-plume regions of GITs and HETs. Various simulations are carried out as a proof of concept to validate the new boundary conditions. Results are demonstrated on both planar and axisymmetric geometries, with parametric sensitivity analyses on the injection ion Mach number as well as on the simulation domain size. Plume properties are characterized and compared against the semi-analytical kinetic solution of the AKILES code[21, 33], to validate the approach, and the kinetic physics of electrons is discussed.

The rest of the paper is organized as follows. Section II introduces the full PIC code and the boundary conditions. The effects of the new boundary conditions are examined in Section III for a one-dimensional (1D) uniform flow and a planar two-dimensional (2D) plasma expansion. This section also tests different simulation domain sizes for planar and axisymmetric models. After that, Section IV compares and discusses the simulation results of planar and axisymmetric plumes. Analyses on the asymptotic electric potential at infinity downstream and, in particular the electron cooling in the plume, are investigated. Finally Section V summarizes the conclusions of this paper. A preliminary version of this work was presented in [34] and a first version of the full PIC code was introduced in [35].

II. PLASMA PLUME MODEL

The present 2D-3V full PIC electrostatic model moves a large number of macro-particles that sample the continuum phase space of hydrogen ions i and electrons e (mass ratio $m_i/m_e = 1836$) in a collisionless, unmagnetized, far-region plasma plume by solving their Newton law of motion with the standard leap-frog Boris's scheme[22, 36, 37]. After each time step, the code weighs the ion and electron density on each node of a Cartesian grid as

$$n_k = \frac{1}{V_{node}} \sum_p w_p S(x_p, z_p), \tag{1}$$

for $k = i, e$, where (x_p, z_p) denotes the position of the p-th macro-particle of the species of interests, w_p is the macro-particle mass, and $S(x_p, z_p)$ is the Ruyten's density-conserving shape factor for particle-grid interpolation associated to the current node with associated volume V_{node}[38]. The ion and electron densities are used to solve for the electric potential ϕ according to the Poisson's equation using a dynamic alternating direction implicit (DADI) algorithm[39],

$$\nabla^2 \phi = \frac{e}{\varepsilon_0}(n_e - n_i). \tag{2}$$

The resulting electric field $\boldsymbol{E} = -\nabla\phi$ is then updated for the next time step.

As sketched in figure 1, the two-dimensional domain is either planar-symmetric or cylindrical-axisymmetric with respect to the $x = 0$ coordinate line. In axisymmetric 2D geometries, particles are moved in 3D space and then projected into the meridional plane to avoid accuracy issues near the axis. As a general rule, more macro-particles are required to maintain a reasonable quantity of particles per cell near the axis[40]. The weighting scheme used retains second-order accuracy in the axisymmetric case.

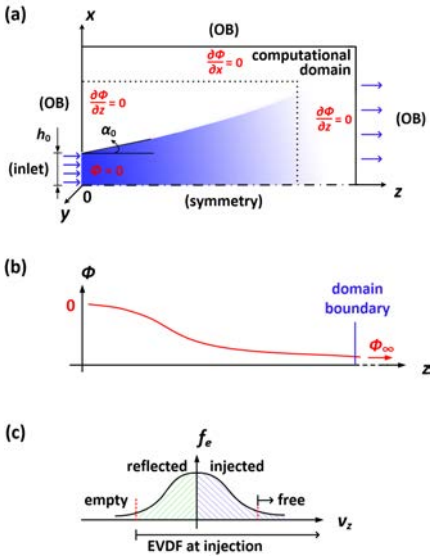

FIG. 1. (a) Geometry of the plasma plume expansion and boundary conditions applied in the computational domain. The plasma plume is initialized within a half-width h_0 and an ion velocity aperture angle at the inlet edge α_0. 20% of the peripheral region, marked by a black dotted line, is removed from the simulation results due to limit the influence of border effects in the electric potential ϕ. (b) As the globally current-free plasma expands, the electric potential decreases monotonically to an asymptote ϕ_∞ far downstream (outside of the computational domain). (c) Sketch of the electron velocity distribution function (EVDF) f_e in the v_z direction at $z = 0$. The function f_e differs from the full Maxwellian, with a cut-off velocity that is related to ϕ_∞ (red dotted lines) marking the injected electrons to be free/reflected above/below this cut-off velocity. As a consequence of this, an empty region exists at high energies for $v_z < 0$.

There are three main types of boundaries in figure 1: the plasma source exit plane at the bottom-left of the domain (inlet); the symmetric plane (or axis) along $x = 0$; and outer boundaries (OBs). At each boundary, the treatment of the electric potential ϕ, electrons e, and ions i, must be specified.

Regarding ϕ, Dirichlet boundary conditions are imposed at the inlet, setting $\phi = 0$ there. Von Neumann conditions are set at the outer boundaries and at the $x = 0$ line, $\partial\phi/\partial\nu = 0$, where ν is the normal direction to the boundary. Strictly speaking, this assumption is appropriate only in the limit of infinitely large simulation domains that cover most of the ϕ fall that takes place in the plasma plume. Therefore, an error associated to the finite domain size arises from this choice of boundary conditions on ϕ. For this reason, the potential map in a conservative 20% of the domain border around the downstream and lateral boundaries (as shown in figure 1) has been disregarded before postprocessing in all figures shown in this work (see Section III C for a discussion of the effects of the domain size).

Regarding electrons and ions, boundary conditions must agree with the current-free condition in the plasma plume. This is consistent with expectation for a plasma thruster operating in free space, but naturally, other, alternative choices for the total emitted current could be made. Since the electric potential in the plume decreases monotonically downstream, and the nearly-monoenergetic ions are much colder than electrons, the treatment of ions and electrons at the boundaries must be consistent with their substantially different behavior.

On the one hand, electrons constitute a nearly-confined population in the plasma plume, with most of the population being reflected back to the plasma source by the potential fall. Only the most energetic electrons are expected to escape downstream, as shown in figure 1(c). Since the reflection of some of the electrons may occur outside of the finite simulation domain, the definition of the boundary conditions both at the inlet and at the outer boundaries must be done with care. This issue is addressed in detail in the next subsection.

On the other hand, ions are injected at the inlet with a uniform density profile and uniform ion Mach number $M_0 = u_i/c_s^*$, where $c_s^* = \sqrt{T_e^*/m_i}$, with T_e^* the reference electron temperature of the near-Maxwellian distribution function in the plasma source. The direction of the velocity vector is chosen such that the angle it forms with the symmetry plane (or the axis), behaves as $\alpha = \alpha_0 x/h_0$, where α_0 is the chosen divergence angle at the plume edge $x = h_0$ (see figure 1). Since ion temperature is usually much smaller than electron temperature in the plasma thruster plume[3, 7, 11], the ion population is assumed cold, and thus is injected with no thermal spread. Since ions are accelerated outward and suffer no backward reflections, no special treatment is required at the outer boundaries, and therefore ions reaching them are simply eliminated.

The resulting model can be normalized with the following parameters: the reference electron temperature at the source T_e^*, the electron mass m_e, the elementary charge e, the ion number density at the inlet n_{i0}, and the characteristic Debye length $\lambda_D^* = \sqrt{\varepsilon_0 T_e^*/(n_{i0}e^2)}$. Typical values of these parameters in a plasma thruster plume range from $T_e^* = 1$ to 5 eV, the peak of n_{i0} in the order of 10^{16} to 10^{18} m^{-3} [3, 9, 12]. Note that the actual electron temperature at $z = 0$, T_{e0}, may differ from the given reference at injection, T_e^*, as the electron velocity distribution function deviates from the reference Maxwellian f_e^M,

$$f_e^M(v_x, v_y, v_z) = n_e^* \left(\frac{m_e}{2\pi T_e^*}\right)^{3/2} \exp\left[-\frac{m_e({v_x}^2 + {v_y}^2 + {v_z}^2)}{2T_e^*}\right], \tag{3}$$

due to the existence of an empty region of high energy electrons with $v_z < 0$, as shown in figure 1(c).

The normalized model depends solely on the initial plasma profile at injection and the numerical domain size, grid size, and time step. The initial profile is characterized by its initial half-width h_0 (given in multiples of the reference Debye length λ_D^*), the ion Mach number M_0, and the ion velocity aperture angle at the inlet edge, α_0, as shown in figure 1. In the following, the dimensionless simulation time-step $\Delta t\omega_{pe_0} = 0.05$ is chosen so that it is much smaller than the inverse of the dimensionless electron plasma frequency[22, 41] $\omega_{pe0} = \sqrt{n_{i0}e^2/(m_e\varepsilon_0)}$. Unless otherwise specified, the plume expansion domain used is $300\lambda_D^* \times 50\lambda_D^*$, with a grid resolution of one Debye length λ_D^*, which allows to perform stable simulations. Upon injection, macro-particles are pre-accelerated for a random time step $0 < \Delta t_{rand} < \Delta t$ to ensure a smooth and uniform plasma injection. Finally, a target number of macro-particles per cell, $N_c \geq 10$ is chosen to keep low noise statistics. Steady state is achieved by running the code for $5\text{–}12 \cdot 10^4$ time steps, far exceeding the ion maximum residence time of $643\text{–}2570\omega_{pe0}^{-1}$ in the domain ($1.3\text{–}5.1 \cdot 10^4$ time steps).

A. Electron boundary conditions

The new electron boundary conditions aim to reproduce the physics of a far region plasma plume, taking into account the nearly-confined nature of the electron population.

Electrons at the injection boundary are sampled from a non-dimensional semi-Maxwellian distribution f_e^M for $v_z > 0$. Since the number of reflected electrons streaming back to the source is unknown a priori, direct injection of electrons with this distribution function can lead to an important mismatch in the ion and electron densities at the inlet. Thus, the magnitude n_e^* of this distribution is adapted in every time step to ensure that the quasineutrality condition is satisfied at the inlet, $n_{i0} = n_{e0}$, taking into account in the weighing the newly emitted macro-particles and those that have been reflected back to the

source and are present in the neighborhood of the inlet. This procedure dynamically modifies the number of injected electrons in every time step until a steady-state is reached.

Regarding the treatment of the outer boundaries, as noted above, a consistent approach must selectively reflect or reinject part of the electrons reaching the outer boundary. Still, screening which electrons ought to be reflected is a challenging task, since the required amount varies as the simulation reaches its steady state. The proposed approach here mimics the partial reflection of electrons that would take place further downstream (outside of the domain), by enforcing the integral current-free condition along the outer edge of the domain, $J_i = J_e$. This is accomplished by ordering the electrons according to their mechanical energy, and tagging the lowest energy electrons for reinjection, so that the number of escaping free electrons equals the number of escaping ions. The threshold energy that divides the reflected from the passing electrons is denoted as the critical reflection energy E_{crit} in the following. This way, only the higher-energy electron population tail is removed from the simulation at each time step, which are the electrons that can escape to infinity to neutralize the ion beam in the steady state.

The critical reflection energy for the domain outer boundaries can be recomputed every time step to decide which electrons to reflect. However, for a practical number of total macro-particles in the simulation, preliminary testing found that this threshold value may fluctuate substantially across several time steps, introducing PIC noise. Therefore, a moving time-average of E_{crit} is used to minimize this issue (see figure 2). An averaging time window in the order of the electron residence time in the domain improves the stability and noise of the simulation. However, this time range of average must keep regular changes to yield a trade-off between the suppression of random noise and convergence speed. Once the steady-state has been reached, the stationary value of the critical energy also indicates the plasma plume potential at infinity, ϕ_∞.

The reinjected electrons are specularly reflected, by inversing the normal v-component to the boundary while keeping other v-components unchanged, without any delay to account for their unknown trip time outside of the domain. While this does affect the transient plume set-up process from the instant where electrons first arrive at the outer boundary until the steady-state is reached, it is hypothesized that it does not alter the steady-state plume solution.

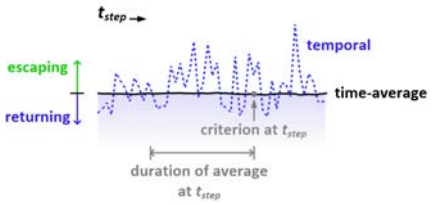

FIG. 2. Sketch of the criterion on selective electron reflection at the outer boundaries. Electrons of an initial energy over the time-average critical level completely escape from the simulation domain; others are reflected back specularly. The duration of the moving average is an additional free numerical parameter of the simulation.

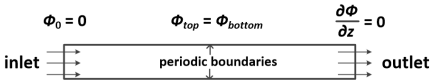

FIG. 3. Sketch of the uniform 1D flow test case. The lateral domain edges use periodic boundary conditions in this case.

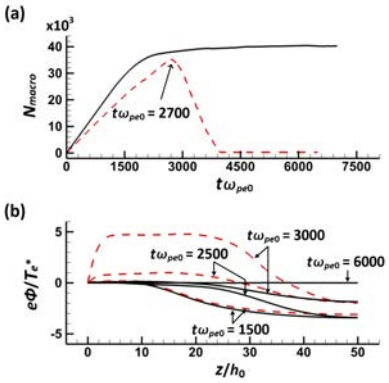

FIG. 4. Evolution of (a) total number of electron macro-particles, (b) electric potential for $M_0 = 5$ under different boundary setups. Red dashed lines stand for the constant-injection, open boundary conditions prevalent in other studies. Black solid lines present the results of the new boundary conditions.

III. BOUNDARY CONDITION TEST AND ANALYSIS

This section demonstrates the performance of the proposed new boundary conditions. A first test case shows the consistency of the approach in a uniform 1D flow without any transverse expansion. Then, a 2D simulation on the (x, z) plane involving transverse expansion is presented. The proposed boundary conditions are compared with the prevalent boundary conditions used in other studies: fixed electron emission at the inlet, regardless of the disparity of densities that arises there as a consequence of reflected electrons, and simple elimination of all macro-particles reaching the domain edge. Finally, we compare various simulations of the same steady-state plasma plume with different domain sizes. The values $M_0 = 5$, $\alpha_0 = 0$ are used as the reference in all test cases.

A. Uniform 1D flow

As shown in figure 3, a planar domain with just 10 grid cells in the x direction and 500 grid cells in the z direction, each one λ_D^* in size, is used to simulate a uniform flow without any lateral expansion. The new boundary conditions are compared against the reference case used in other studies: constant electron injection, and simple removal of all particles reaching the outer boundary. Plasma parameters in this test are plotted in figure 4 as a function of time. One can see from panel (a) that the number of electron macro-particles keeps a similar increase for both simulations in the beginning, almost until $t\omega_{pe0} = 1500$. During this early stage, the electric potential distributes similarly for both sets of boundary conditions, as seen in panel (b).

The simulation with the new boundary conditions then converges to a total number of electron macro-particles in the domain and to the expected flat electric potential in the absence of expansion. However, the total number of electrons peaks for the reference simulation around $t\omega_{pe0} = 2700$ (a duration lower than the characteristic residence time of ions) and then decreases until only a few hundreds of electrons are left in the domain. This final state is due to the accumulation of positive charge in the domain, and a resulting positive ϕ at the boundary downstream, which makes all newly injected particles to quickly abandon the domain.

The distinction of ϕ between two simulations is clearly visible from $t\omega_{pe0} = 2500$ onward. While the new boundary conditions result in a flat potential at large times (as expected in uniform flow), a positive potential jump appears adjacent to the injection plane under the reference boundary conditions. The profile of ϕ at later times in the reference simulation (not shown) becomes unstable, its positive sign rising steadily not only near the entrance, but also downstream.

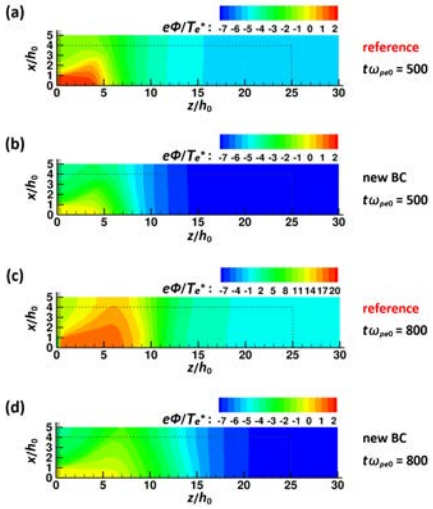

FIG. 5. Electric potential in the (x, z) plane for $M_0 = 5$ at (a) $t\omega_{pe0} = 500$ under the reference, (b) $t\omega_{pe0} = 500$ under new BC, (c) $t\omega_{pe0} = 800$ under the reference, and (d) $t\omega_{pe0} = 800$ under new BC. The dotted line indicates the last 20% of the simulation domain in the x and z directions that is disregarded in the rest of the figures of this work. Notice the different color scale in plot (c) to accommodate the large potential rise.

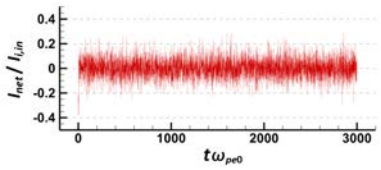

FIG. 6. Relative net current at the inlet, $I_{net} = I_i - I_e$, normalized with the injected ion current.

B. 2D planar expansion

The basic model in this test conforms to figure 1 with initial half-width $h_0 = 10\lambda_D^*$ and divergence angle $\alpha_0 = 0$. After $t\omega_{pe0} = 500$, figures 5(a) and (b), the electric potential maps show a gradual spatial drop from the peak at the beam core to the plume edge, although a quite different peak value occurs for the two simulation cases (reference and new boundary conditions). While the new boundary conditions have a monotonic potential fall, as expected in a plasma plume, a positive plasma sheath is already visible at the inlet under the reference boundary conditions, which continues to grow at later times to a large positive potential due to a strong non-neutrality that develops near the inlet due to the fixed-current injection of electrons. This effect, together with the effect of the boundary conditions on ϕ in this case, is believed to explain the sheath observed in [28]. As the plasma expands subsequently, at e.g. $t\omega_{pe0} = 800$ in panels (c) and (d), under the reference boundary conditions a large positive potential region appears that reaches into the lateral boundary, confining ions and leaking electrons out of the domain, reinforcing the positive potential growth inside the plume and quickly becoming unstable. On the contrary, the evolution of the potential with the new boundary conditions is smooth and does not present these nonphysical features.

In the steady state, the simulation with the new bound-

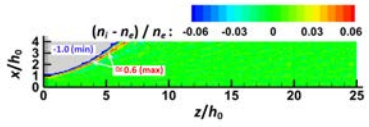

FIG. 7. Non-neutrality ratio for the planar plume with $M_0 = 5$ during the steady state under the new boundary conditions. 20% of the simulation domain around the downstream and lateral outer boundaries is removed from the plots.

ary conditions exhibits a net current crossing the inlet that fluctuates about zero, as shown in figure 6. The relative number density difference between ions and electrons plotted in figure 7 shows that the plume is essentially quasineutral except at the plume edge.

Finally, it is noted that the new boundary conditions do not produce artifacts at injection such as artificial sheath, which are typical of the reference boundary conditions. Such sheath is visible in figure 5 (a) and (c).

C. Sensitivity to the simulation domain size

Next, to understand the effect of the domain size, the general computational domain is reduced to 40%, 60% and 80% of the original length of figure 1 and for $M_0 = 5$ in both planar and axisymmetric cases. It is noted that in all simulations, a 20% of the domain is still cut out to prevent border effects on ϕ.

Overall, excellent consistency is observed in both cases, in the light of the electron number density and the electric potential plots of figure 8. Nonetheless, a small domain size effect is visible as a difference in $e\phi/T_e^*$ between the different simulations, which accounts to up to a 5% of the total potential drop. These results further support the validity of the new boundary conditions to compute a steady-state plasma plume section regardless of the domain size.

IV. INVESTIGATION OF THE PLASMA PLUME EXPANSION

In the following, both 2D planar and axisymmetric plasma plume simulations are presented and discussed to further demonstrate the application of the new boundary conditions and to explore several aspects of plasma plume physics. The simulations correspond to the domain shown in figure 1. Results correspond to time averages over 10^4 time steps in the steady state to reduce statistical noise.

A. Macroscopic plume structure

Two-dimensional maps of the ion plume number density are plotted in figure 9 for planar and axisymmetric cases, respectively, and three initial ion Mach numbers M_0. The initial injection profile is purely axial, i.e., $\alpha_0 = 0$. As the plasma expands laterally, a fanning plume structure gradually forms. The transverse plasma expansion occurs due to the residual electron pressure, which competes with ion inertia to increase the beam width; the effect is therefore more noticeable at lower ion Mach numbers M_0, in agreement with the results of fluid models[15].

The monotonically-decreasing maps of n_i and ϕ are consistent with those of previous fluid and kinetic studies[42]. While the density profile at the inlet is uniform, a lateral density gradient develops downstream as a consequence of the transverse expansion. This spatial expansion is larger the lower M_0 is. The initial Mach number M_0 governs most of the characteristics of the plume expansion. Indeed, the Mach line that starts at the inlet edge (and carries the information of the expansion into the plasma), whose slope is given by $-\arcsin(1/M_0)$, intersects the $x = 0$ line at $z/h_0 \simeq 4.90$ for $M_0 = 5$, $z/h_0 \simeq 9.95$ for $M_0 = 10$ and $z/h_0 \simeq 19.97$ for $M_0 = 20$, forming a nearly-uniform density core in the lower left part of the plots. Thus, as M_0 is increased, the region of larger density near the axis extends further downstream. It is evident that the density drop occurs faster in axisymmetric plumes than in planar plumes, as the former involves the expansion in two perpendicular directions (x, y) while the latter only in one (x). Taking the case of $M_0 = 5$ for instance, n_i/n_{i0} drops by two orders of magnitude at $z/h_0 = 25$ during the axisymmetric expansion but by just one order of magnitude in the planar plume.

Figure 10 shows the 2D profiles of the steady-state plasma electric potential for the planar and axisymmetric plumes. The electric potential drops monotonically laterally and downstream, confining electrons. The total potential fall is larger the smaller the initial ion Mach number M_0 is, and takes place in a shorter distance from the inlet. The potential fall occurs closer to the plasma source in the axisymmetric case, consistent with the faster drop in density.

TABLE I. Asymptotic electric potential $-e\phi_{\infty,average}/T_e^*$ in each case.

MODEL	$M_0 = 5$	$M_0 = 10$	$M_0 = 20$
planar	2.6	1.9	1.1
axisymmetric	2.9	2.1	1.2

B. Asymptotic electric potential

As demonstrated above, the new boundary conditions allow obtaining the stable solution of the steady state plume expansion. The critical reflection energy E_{crit} for the electrons associated to the outer boundaries reaches a stationary value, from which the asymptotic potential value $\phi_\infty = -E_{crit}/e$ far downstream can be computed. Table I shows the asymptotic potential for the six simulations. The time to reach the asymptotic electric potential $e\phi_\infty/T_e^*$ scales with the ion residence time in the simulation domain, and therefore, the process takes longer the lower M_0. The time-averaging technique of Section II has been used to filter the variations that would otherwise take place during the transient plume set-up, shown in Figure 11 The total potential fall in the plume $|e\phi_\infty/T_e^*|$ decreases the larger M_0 is, allowing more electrons to escape to infinity. This trend is consistent with the direct-Vlasov kinetic results of reference [21].

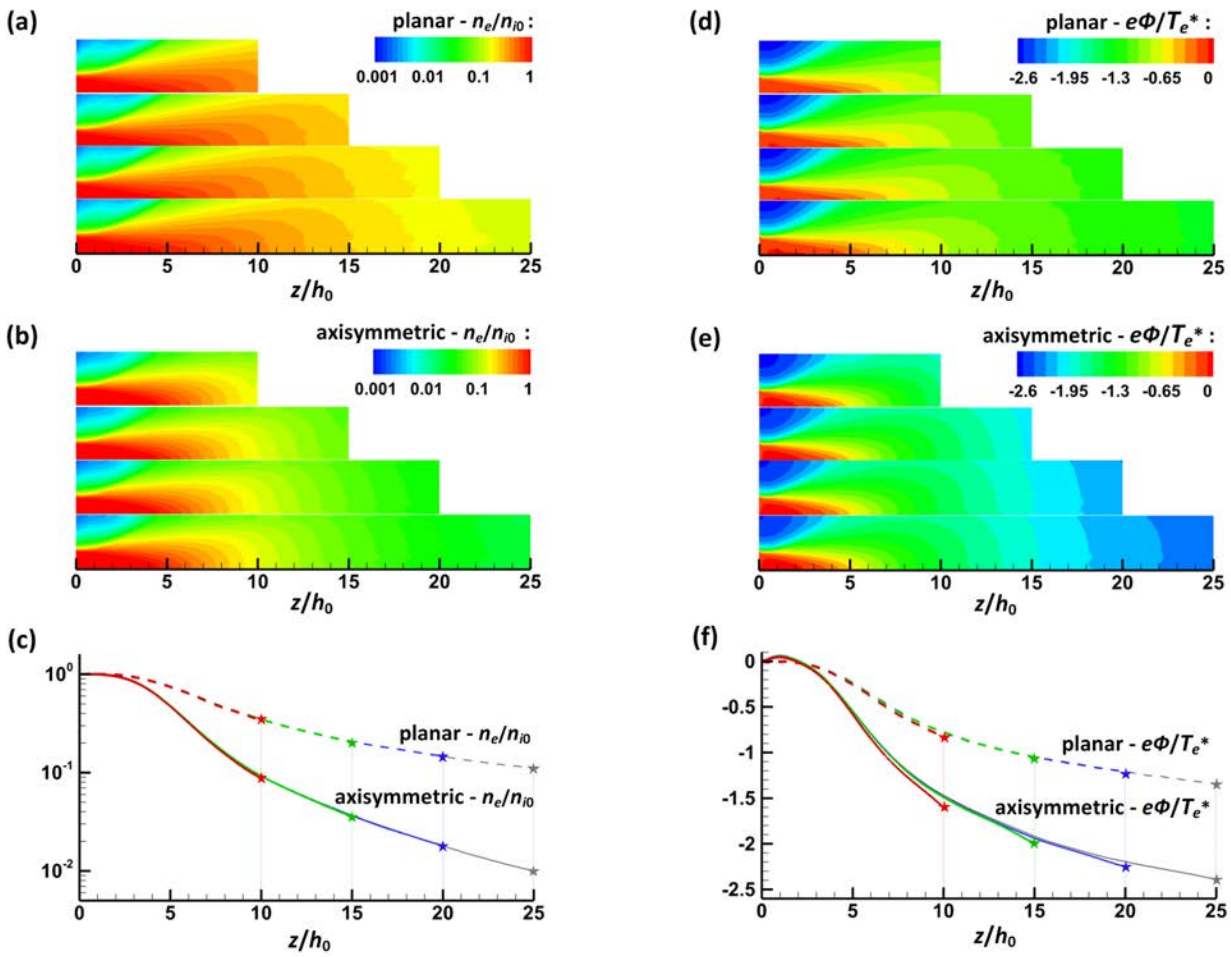

FIG. 8. Electron number density and electric potential for $M_0 = 5$ from simulations with 40%, 60% and 80% lengths of the general domain. 2D views of n_e/n_{i0} are compared on (a) planar and (b) axisymmetric configurations. (c) 1D profiles of n_e/n_{i0} are extracted along the central z-axis and practically overlap in both planar (solid lines) and axisymmetric (dashed lines) cases. 2D views of $e\phi/T_e^*$ are compared on (d) planar and (e) axisymmetric configurations. (f) 1D profiles of $e\phi/T_e^*$ are extracted along the central z-axis and practically overlap in the planar (dashed lines) cases, while appear errors in the axisymmetric (solid lines) cases. The asterisks in plots (c) and (f) designate the far end each computational domain. In each case, 20% of the domain around the downstream and lateral outer boundaries is removed from the simulation.

TABLE II. Polytropic cooling rates along the central streamline in each case.

MODEL		$M_0 = 5$	$M_0 = 10$	$M_0 = 20$
planar	γ_x	1.762	1.792	2.021
	γ_z	1.209	1 .218	1.595
	γ	1.188	1.209	1.387
axisymmetric	γ_x	1.513	1.585	1.768
	γ_z	1.146	1 .127	1.267
	γ	1.296	1.318	1.508

C. Electron cooling and velocity distribution function

The semi-confined, collisionless electron population is not in local thermodynamic equilibrium. Rather, the electron response is *global*, as features in one location (such as the presence of an absorbing boundary condition, or the value of ϕ_∞), affect the electron distribution function everywhere. The lack of full confinement means that the electron species can not be described with an isothermal law; the lack of local thermodynamic equilibrium (due to a large Knudsen number) means that other common closure relations (polytropic, adiabatic) are not physically justified, either. A kinetic model, like the present one, is thus required to analyze the evolution of the electron temperature, and its anisotropy, in the plasma plume.

Figure 12 plots the electron temperature components T_{ex}/T_e^*, T_{ey}/T_e^*, and T_{ez}/T_e^* along $x = 0$ for both planar and axisymmetric cases (in the axisymmetric cases, T_{ex} is the radial component and T_{ey} is the azimuthal component). In both cases, a small initial anisotropy can al-

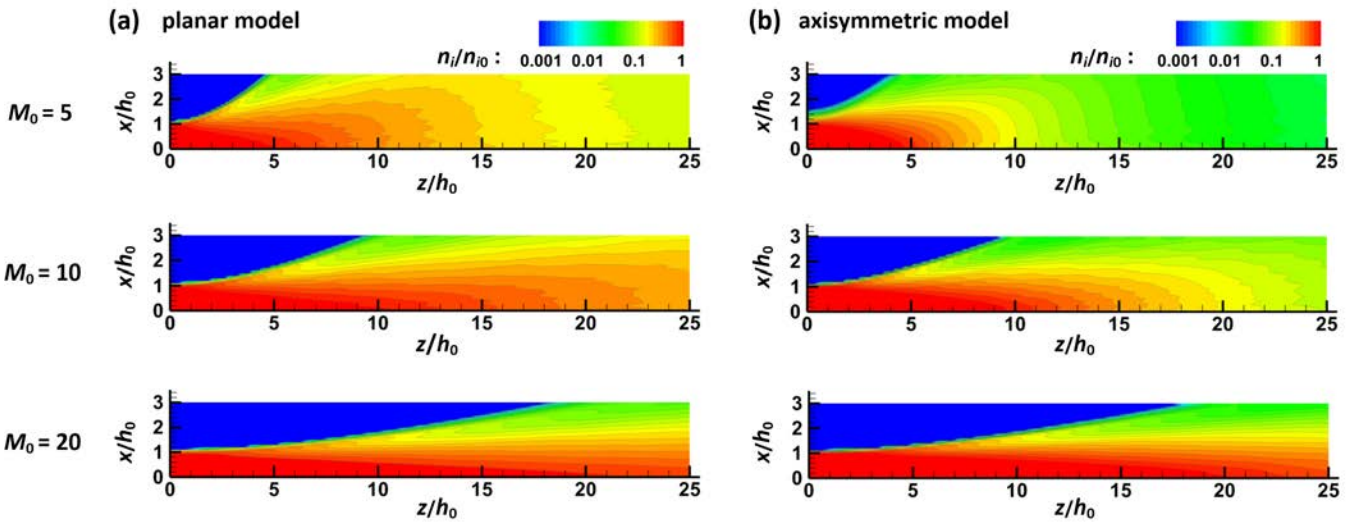

FIG. 9. Ion number density contours for $M_0 = 5$, $M_0 = 10$ and $M_0 = 20$ from (a) planar and (b) axisymmetric models. Thin solid lines correspond to contour lines.

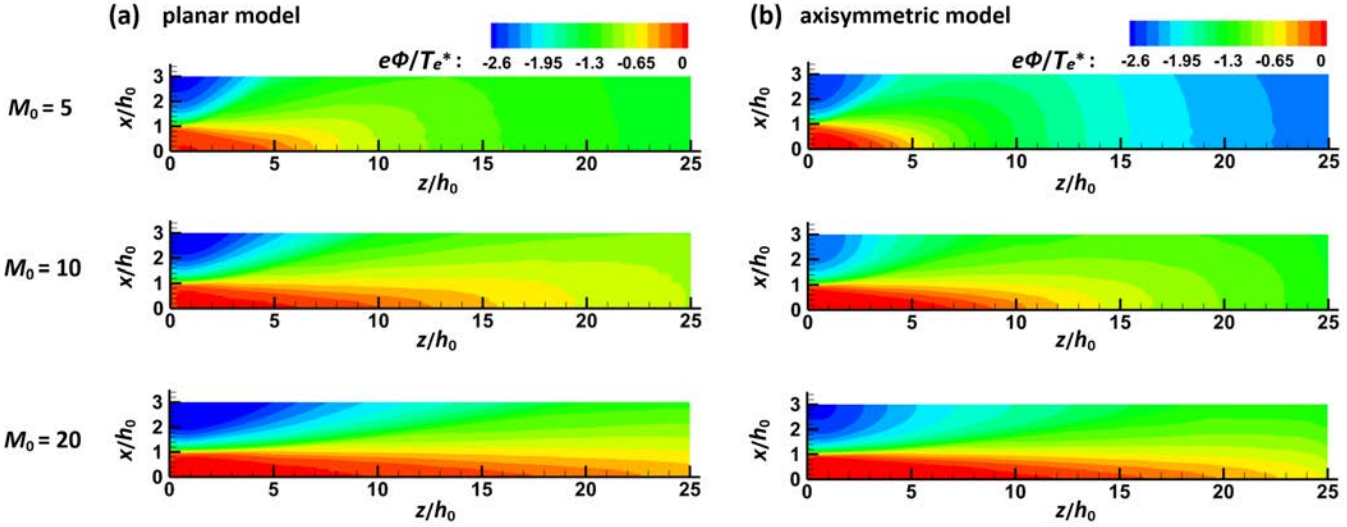

FIG. 10. Electric potential contours for $M_0 = 5$, $M_0 = 10$ and $M_0 = 20$ from (a) planar and (b) axisymmetric models.

ready be observed at the inlet: this is due to the electron velocity distribution function not being fully Maxwellian at injection because of the non-existence of high-energy reflected electrons.

In the planar plume, the motion in the y direction is trivial and unchanging, and thus T_{ey} remains constant. In axisymmetric plasma plumes, however, $T_{ey} = T_{ex}$. The other components of electron temperature decrease monotonically in the z direction in either case. In overall, T_{ex} (and T_{ey} in the axisymmetric case) presents a quicker drop than T_{ez} and the average electron temperature T_e, which is defined as

$$T_e = \frac{T_{ez} + T_{ex} + T_{ey}}{3}. \tag{4}$$

Consequently, the initial electron anisotropy increases downstream as the local fraction of reflected and free electrons changes with z. The dependency with M_0 is clear in the simulations: the higher M_0, the slower the plume electrons cool down. Lastly, observe that the computed value of T_{e0} at the source exit is always slightly smaller than the reference value T_e^*. This is another consequence of the incomplete reflection of emitted electrons.

Figure 13 displays the 2D maps of the electron temperature components T_{ex}, T_{ez}, and the average temperature

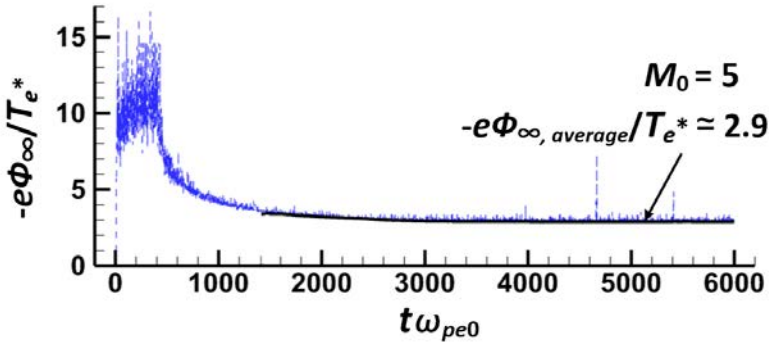

FIG. 11. Asymptotic electric potential downstream for $M_0 = 5$ from the axisymmetric model. The blue dashed line is derived from the instantaneous energy criterion on electron selection at OBs. The black solid line is obtained through averaging at regular intervals after the bulk of ion plume reaching the downstream edge.

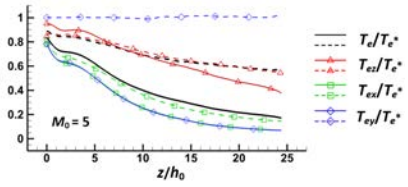

FIG. 12. Electron temperature profiles extracted along the plume z-axis for $M_0 = 5$. Planar and axisymmetric results are plotted by dashed and solid lines respectively. The black lines without symbol represent the average T_e/T_e^*, while other signed lines represent T_{ez}/T_e^* (red triangles), T_{ex}/T_e^* (green rectangles), and T_{ey}/T_e^* (blue diamonds) for corresponding models.

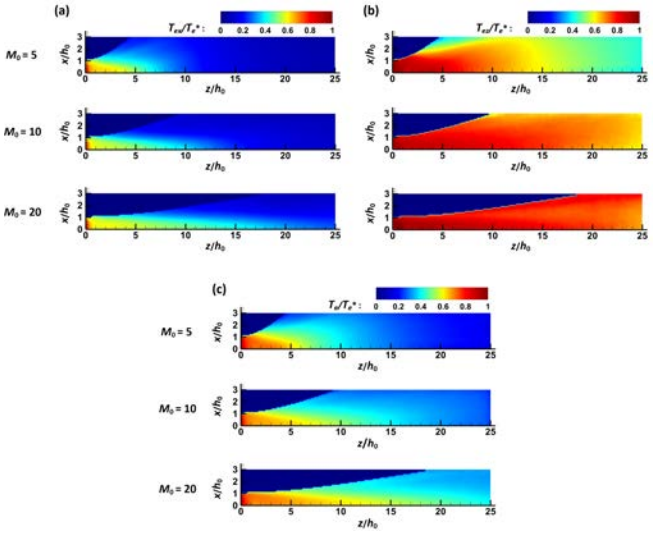

FIG. 13. Electron temperature in the axisymmetric plume for three values of the initial Mach number M_0. Columns (a), (b) and (c) show the lateral temperature T_{ex}/T_e^*, axial temperature T_{ez}/T_e^*, and average temperature T_e/T_e^*, respectively.

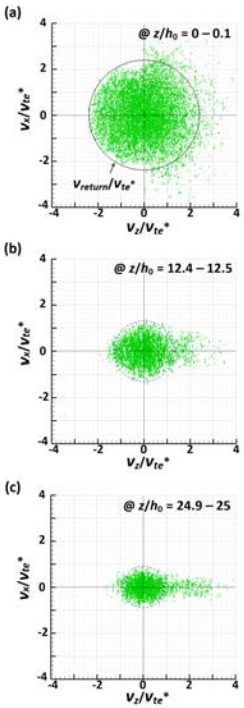

FIG. 14. Scatter diagrams of the electron velocity distribution at different positions of z/h_0, from the axisymmetric model for $M_0 = 5$. Plot (a) sketches the thin black circle labeled with v_{return} according to the energy criterion to reflect electrons in figure 11. Thin dashed blue circles in other plots indicates the critical energy E_{crit}. Velocity $v_{te}^* = \sqrt{T_e^*/m_e}$ is the dimensionless reference electron thermal velocity.

T_e for the axisymmetric plasma plume, for three values of the initial ion Mach number M_0. The faster cooling rate of T_{ex} compared to T_{ez} is apparent in all three cases. A larger M_0 results in a slower cooling rate. Interestingly, while the temperature components are laterally uniform at the plasma source, a lateral gradient of electron tem-

perature develops downstream, with peripheral electrons cooling faster than axial electrons. This gradient was not observed in the quasi-1D kinetic model of [21], where a different initial plasma density profile was used.

These results illustrate that the expansion of a hypersonic plasma plume is neither isothermal nor isotropic. Notwithstanding this, it is desirable to find approximated polytropic relations $T_{ek}/{n_e}^{\gamma-1} = \text{const}$, where $k = x, y, z$, to quantify the overall electron cooling rate. As shown in table II, the fitted polytropic exponents γ along the central streamline differ for each electron temperature component. Increasing M_0 results in larger average γ values, from about 1.2–1.3 for $M_0 = 5$ to 1.4–1.5 for $M_0 = 20$. In agreement to preceding results, γ_x is larger than γ_z, indicating that T_{ex} cools down faster than T_{ez}. Furthermore, the cooling rates are higher in the axisymmetric cases than in the planar cases in general. It is stressed that the single-polytropic fit for each electron temperature component provided here is only an approximation: this trend lines fail to match the behavior of the electron temperature in the initial part of the plume expansion and far downstream. The good quality of the fit in the present simulations is partially due to the reduced length of the domains under consideration. Importantly, the directional temperatures T_{ex} and T_{ez} are fitted by different politropic exponents, indicating the anisotropy that develops in the plume in the electron population.

Lastly, figure 14 displays the evolution of the electron velocity distribution function along the $x = 0$ line in the $v_x - v_z$ plane for the axisymmetric $M_0 = 5$ case only. This figure can be qualitatively compared with figure 5 of reference [21]. Steady-state scatter diagrams are derived at the plume central z-axis adjacent to the source entrance ($z/h_0 = 0$–0.1), the intermediate section ($z/h_0 = 12.4$–12.5) and the downstream edge of domain ($z/h_0 = 24.9$–25), respectively. In each plot, the electron distribution is asymmetric with respect to the $v_z = 0$ axis, consistent with the absence of high-energy reflected electrons. The symmetric part of the distribution function where reflected electrons exist has been enclosed in a circular line, which corresponds to the critical reflection energy E_{crit} used in the new outer boundary model. As the expansion proceeds and the electric potential decreases and approaches ϕ_∞, the radius of this circle becomes smaller. The electron subpopulation beyond this line are the free electrons. As it can be observed, these free electrons, which at the inlet are present all over the $v_z > 0$ space due to the semi-Maxwellian injection law, cluster around the $v_x = 0$ axis further downstream, while a new empty region emerges on $v_z > 0$ for large values of $|v_x|$. This behavior is associated to the transformation of radial kinetic energy into axial kinetic energy as the electrons bounce radially back and forth in the electric potential hill that exists along the plume axis, and is related to the increase of electron anisotropy and the differentiated cooling rates of T_{ex} and T_{ez}. As discussed in [21], this bouncing motion and the conversion of radial to axial energy is associated with the conservation of an invariant action integral.

V. CONCLUSIONS

A full PIC simulation model with physically-consistent boundary conditions for the electron population has been presented to characterize unmagnetized, collisionless plasma plumes expanding into vacuum. The new boundary conditions enforce the global current-free condition in the plume and quasineutrality at the injection plane. The model has been shown to simulate stably the plasma plume steady state, with good agreement with fluid and 1D-kinetic previous models, and good independence of the chosen domain size. The boundary conditions thus are an improvement over the prevailing ones used in other codes.

The model has been used to study planar and axisymmetric plasma plumes, recovering the plasma density and electric potential fall, as well as the evolution of the anisotropic temperature of the electrons. The asymptotic value of the electric potential far downstream, ϕ_∞, and the electron collisionless cooling rates have been analyzed. The initial ion Mach number M_0 is a fundamental plume parameter that determines the magnitude and rate of the electric potential fall in the plume, and with it, all other aspects including the plume lateral divergence rate. A higher M_0 (i.e., a more hypersonic plume) results in a less-divergent expansion, a smaller potential fall, and a lower rate of change of all variables. This trend reveals the importance of the rate of electron thermal energy to ion kinetic energy in the plume.

The electrons are a nearly-confined species, with only a small subpopulation of fast free electrons escaping downstream and neutralizing the ion beam. The electron distribution function is anisothermal and anisotropic, even when the plasma inlet injects semi-Maxwellian electrons as illustrated here. The fitted, approximated polytropic cooling exponents for the electron temperature components show a fast cooling rate of the transverse temperature, and a slower cooling rate of the axial temperature.

Further work will extend the present model to include real effects of plasma plume expansion, such as a background magnetic field, warm ions, initial velocity distribution functions other than Maxwellian, and collisional interactions.

ACKNOWLEDGMENTS

Min Li's work has been supported by the National Natural Science Foundation of China (Grant No. 11872093). Mario Merino and Eduardo Ahedo's work has been supported by the Spanish R&D National Plan under grant number ESP2016-75887-P.

[1] R.I.S. Roy, N.A. Gatsonis, and D.E. Hastings. Ion-thruster plume modeling for backflow contamination. *Journal of Spacecraft and Rockets*, 33(4):525–534, July 1996. doi:10.2514/3.26795.

[2] F Darnon. Plume effects in plasma propulsion, an overview of cnes activities. In *Spacecraft Propulsion*, volume 465, page 693, 2000.

[3] Dan M. Goebel and Ira Katz. *Fundamentals of Electric Propulsion: Ion and Hall Thrusters*. John Wiley & Sons, 2008.

[4] M.A. Lieberman and A.J. Lichtenberg. *Principles of plasma discharges and materials processing*. Wiley-Blackwell, 2005.

[5] K.F. Schoenberg, R.A. Gerwin, R.W. Moses, J.T. Scheuer, and H.P. Wagner. Magnetohydrodynamic flow physics of magnetically nozzled plasma accelerators with applications to advanced manufacturing. *Physics of Plasmas*, 5(5):2090–2104, 1998.

[6] M.W. Liemohn and G.V. Khazanov. Collisionless plasma modeling in an arbitrary potential energy distribution. *Physics of plasmas*, 5(3):580–589, 1998.

[7] David Manzella and John Sankovic. Hall thruster ion beam characterization. In *31st Joint Propulsion Conference and Exhibit*, page 2927, 1995.

[8] V.V. Zhurin, H.R. Kaufman, and R.S. Robinson. Physics of closed drift thrusters. *Plasma Sources Science and Technology*, 8(1), 1999.

[9] R.M. Myers and D.H. Manzella. Stationary plasma thruster plume characteristics. In *23rd International Electric Propulsion Conference, Seattle, WA*, IEPC 93-096, 1993.

[10] J. Wang, D. Brinza, and M. Young. Three-Dimensional Particle Simulations of Ion Propulsion Plasma Environment for Deep Space 1. *Journal of Spacecraft and Rockets*, 38(3):433–440, May 2001. URL: http://doi.aiaa.org/10.2514/2.3702, doi:10.2514/2.3702.

[11] I.D. Boyd and R.A. Dressler. Far field modeling of the plasma plume of a Hall thruster. *Journal of applied physics*, 92(4):1764, 2002.

[12] B.E. Beal, A. Gallimore, and J.M. Haas W.A. Hargus. Plasma properties in the plume of a hall thruster cluster. *Journal of Propulsion and Power*, 20(20):985 – 991, 2004.

[13] L. Brieda M.R Nakles, W.A Jr Hargus D. R. Garrett, and R.L. Randy. Experimental and numerical examination of the BHT-200 Hall thruster plume. In *43rd AIAA/ASME/SAE/ASEE Joint Propulsion Conference & Exhibit*, page 5305, Washington DC, 2007. AIAA.

[14] K Dannenmayer and Stéphane Mazouffre. Electron flow properties in the far-field plume of a hall thruster. *Plasma Sources Science and Technology*, 22(3):035004, 2013.

[15] Mario Merino, Filippo Cichocki, and Eduardo Ahedo. Collisionless plasma thruster plume expansion model. *Plasma Sources Science and Technology*, 24(3):035006, 2015. doi:10.1088/0963-0252/24/3/035006.

[16] J. Denavit. Collisionless plasma expansion into a vacuum. *The Physics of Fluids*, 22(7):1384–1392, 1979.

[17] Douglas B VanGilder, Gabriel I Font, and Iain D Boyd. Hybrid monte carlo-particle-in-cell simulation of an ion thruster plume. *Journal of Propulsion and Power*, 15(4):530–538, 1999.

[18] AG Korsun, EM Tverdokhlebova, and FF Gabdullin. Mathematical model of hypersonic plasma flows expanding in vacuum. *Computer physics communications*, 164(1-3):434–441, 2004.

[19] F Taccogna, D Pagano, F Scortecci, and A Garulli. Three-dimensional plume simulation of multi-channel thruster configuration. *Plasma Sources Science and Technology*, 23(6):065034, 2014.

[20] E Camporeale, EA Hogan, and EA MacDonald. Approximate semi-analytical solutions for the steady-state expansion of a contactor plasma. *Plasma Sources Science and Technology*, 24(2):025014, 2015.

[21] Mario Merino, Javier Mauriño, and Eduardo Ahedo. Kinetic electron model for plasma thruster plumes. *Plasma Sources Science and Technology*, 27(3):035013, 2018. doi:10.1088/1361-6595/aab3a1.

[22] C.K. Birdsall and A.B. Langdon. *Plasma Physics via Computer Simulation*. Institute of Physics Publishing, Bristol, 1991.

[23] D.Y. Oh, D.E. Hasting, C.M. Marrese, J.M. Haas, and A.D. Gallimore. Modeling of stationary plasma thruster-100 thruster plumes and implications for satellite design. *J. Propulsion Power*, 15(2):345–357, 1999.

[24] Murat Celik, Mark Santi, Shannon Cheng, Manuel Martinez-Sanchez, and Jaime Peraire. Hybrid-PIC simulation of a hall thruster plume on an unstructured grid with DSMC collisions. In *28th International Electric Propulsion Conference*, pages 17–20, 2003.

[25] Alejandro Lopez Ortega, Ira Katz, Ioannis G Mikellides, and Dan M Goebel. Self-consistent model of a high-power hall thruster plume. *IEEE Transactions on Plasma Science*, 43(9):2875–2886, 2015.

[26] Filippo Cichocki, Adrián Domínguez, Mario Merino, and Eduardo Ahedo. Hybrid 3D model for the interaction of plasma thruster plumes with nearby objects. *Plasma Sources Science and Technology*, 26(12):125008, 2017. doi:10.1088/1361-6595/aa986e.

[27] M. Martínez-Sánchez and E. Ahedo. Magnetic mirror effects on a collisionless plasma in a convergent geometry. *Physics of Plasmas*, 18, 2011.

[28] O. Chang J. Wang and Y. Cao. Electron–ion coupling in mesothermal plasma beam emission: Full particle pic simulations. *IEEE transactions on plasma science*, 40:230–236, 2012.

[29] Y. Hu and J. Wang. Electron properties in collisionless mesothermal plasma expansion: Fully kinetic simulations. *Plasma Science, IEEE Transactions on*, 43(9):2832–2838, 2015. doi:10.1109/TPS.2015.2433928.

[30] Adrian Wheelock, David L Cooke, and Nikolaos A Gatsonis. Investigation of ion beam neutralization processes with 2D and 3D PIC simulations. *Computer physics communications*, 164(1-3):336–343, 2004.

[31] Lubos Brieda and Joseph Wang. Modelling ion thruster beam neutralization. In *41st AIAA/ASME/SAE/ASEE Joint Propulsion Conference & Exhibit*, page 4045, 2005.

[32] Lubos Brieda. Model for steady-state fully kinetic ion beam neutralization studies. *IEEE Transactions on Plasma Science*, 46(3):556–562, 2018.

[33] Mario Merino and Javier Mauriño. AKILES code: Advanced Kinetic Iterative pLasma Expansion Solver 2D, 2017. doi:10.5281/zenodo.1098432.

[34] Min Li, Mario Merino, Eduardo Ahedo, Junxue Ren, and Haibin Tang. Full-PIC code validation and comparison against fluid models on plasma plume expansions. In *35th International Electric Propulsion Conference*, number 230, 2017.

[35] Min Li, Hai-Bin Tang, Jun-Xue Ren, and Thomas M York. Modeling of plasma processes in the slowly diverging magnetic fields at the exit of an applied-field magnetoplasmadynamic thruster. *Physics of Plasmas*, 20(10):103502, 2013.

[36] Jay P Boris. Relativistic plasma simulation-optimization of a hybrid code. In *Proc. Fourth Conf. Num. Sim. Plasmas, Naval Res. Lab, Wash. DC*, pages 3–67, 1970.

[37] JW Eastwood and RW Hockney. Computer simulation using particles. *New York: Mc GrawHill*, 1981.

[38] Wilhelmus M Ruyten. Density-conserving shape factors for particle simulations in cylindrical and spherical coordinates. *Journal of Computational Physics*, 105(2):224–232, 1993.

[39] DW Hewett, DJ Larson, and S Doss. Solution of simultaneous partial differential equations using dynamic adi: Solution of the streamlined darwin field equations. *Journal of Computational Physics*, 101(1):11–24, 1992.

[40] Adrián Domínguez, Filippo Cichocki, Mario Merino, Pablo Fajardo, and Eduardo Ahedo. Axisymmetric plasma plume characterization with 2d and 3d particle codes. *Plasma Sources Science and Technology*, 27(10):104009, 2018. doi:10.1088/1361-6595/aae702.

[41] John P Verboncoeur. Particle simulation of plasmas: review and advances. *Plasma Physics and Controlled Fusion*, 47(5A):A231, 2005.

[42] Filippo Cichocki, Mario Merino, Eduardo Ahedo, Yuan Hu, and Joseph Wang. Fluid vs pic modeling of a plasma plume expansion. In 34^{th} *International Electric Propulsion Conference*, number IEPC-2015-420, Fairview Park, OH, 2015. Electric Rocket Propulsion Society.